In lupus nephritis, specific *in situ* inflammatory states are associated with refractory disease and progression to renal failure

Authors

Rebecca Abraham[1] *, Madeleine Durkee[1,2]*, Junting Ai[1], Margaret Veselits[1], Gabriel Casella[1,2], Yuta Asano[1], Anthony Chang[3], Kichul Ko[1], Charles Oshinsky[1], Emily Peninger[1], Maryellen Giger[2] and Marcus R. Clark[1].

Affiliations

Section of Rheumatology[1], Department of Radiology[2] and Department of Pathology[3], University of Chicago, IL, USA, 60637

*authors contributed equally to this work

Correspondence: mclark@uchicago.edu and m-giger@uchicago.edu

Summary

In human lupus nephritis (LN), tubulointerstitial inflammation (TII) on biopsy predicts progression to end stage renal disease (ESRD). However, while approximately half of patients with moderate or severe TII develop ESRD, half do not. Therefore, we hypothesized that TII is heterogeneous with distinct inflammatory states each associated with different renal outcomes. We interrogated renal biopsies from LN longitudinal and cross-sectional cohorts using both conventional and highly multiplexed confocal microscopy. To accurately segment cells across whole biopsies, and to understand their spatial relationships, we developed unique computational pipelines by training and implementing several deep learning models and other computer vision techniques. Surprisingly, across biopsies, high B cell densities were strongly associated with protection from ESRD. In contrast, CD4- T cell population densities, which included CD8, $\gamma\delta$ and double negative (CD4-CD8-δ-, DN) T cells, were associated with both acute refractory renal failure and progression to ESRD. Interestingly, inflammation was organized into different discrete clusters or neighborhoods each with unique characteristics including enrichment for specific cell populations. B cells were often organized into large neighborhoods with CD4+ T cells including T follicular helper-like cells. In contrast, the CD4- T cell populations formed small cellular neighborhoods whose frequency predicted subsequent progression to ESRD. These data reveal that in LN, specific *in situ* inflammatory states are associated with refractory disease and progression to ESRD.

Acknowledgments

Introduction

For over 50 years systemic lupus erythematosus (SLE) has been thought to result from a break in systemic tolerance and production of pathogenic autoreactive antibodies[1,2]. This canonical model is based on extensive studies of patient blood and spontaneous SLE-like animal models. In the kidney, the manifestation of systemic autoimmunity is glomerulonephritis (GN). Indeed, LN is usually equated with GN[3]. However, tubulointerstitial inflammation (TII)—and not GN—predicts progression to end stage renal disease (ESRD)[4-7].

Lupus TII is associated with a local immune response very different than inflammation that is observed in glomeruli. Indeed, while TII is associated with infiltrating B cells, plasma cells, T follicular helper (Tfh) cells, plasmacytoid dendritic cells (pDCs) and myeloid dendritic cells (mDCs), all of these cells are rare in LN glomeruli[8-13]. The immune cells found in TII are often organized into lymphoid-like architectures associated with local antigen-driven B cell clonal selection[12,13]. Therefore, in TII there are complex, intrinsic immune landscapes associated with progressive renal injury. Many of these features are not replicated in mice[14-17]. There is therefore a compelling need to understand *in situ* immunity in human lupus nephritis.

An initial roadmap to the lupus kidney was provided by the Accelerating Medicines Partnership (AMP)-funded single cell RNA-Sequencing (scRNA-Seq) of cells sorted from LN biopsies[18,19]. In one analysis[18], a total of 21 immune cell clusters were observed. While these AMP investigations are informative, there are several limitations. The patient sample was small, and the frequency of each immune cell population has not been related to relevant histological features or clinical states. A larger deficiency of scRNA-Seq is that all spatial information is lost; we do not know how populations spatially relate to each other in the kidney. In addition to losing regional behaviors, this lack of spatial information prevents potential functional relationships from being identified.

Previously, in lupus TII we have used conventional immunofluorescence microscopy coupled to evolving computational and machine learning approaches (Cell Distance Mapping) to characterize the frequency of specific cell populations and identify cell:cell behaviors indicative of cognate

3

immunity[10,11,20]. However, a systemic analysis of TII and identification of prognostic features has been historically impeded by the complexities of analyzing immunofluorescence data from chronically-inflamed kidneys, including tissue autofluorescence due to scarring and patient heterogeneity. Artificial intelligence algorithms have led to significant progress in automated detection and analysis of cells in confocal images[21-24]. These approaches are beginning to be successfully used in cancer biopsy image analysis[25]. However, conventional methods for cell detection and segmentation are not necessarily generalizable to chronically inflamed, complex organs.

Herein, we describe multiple computational pipelines employing several deep learning algorithms that provide high-throughput assessments of cell phenotypes and cellular architectures. These methods have been developed and validated in LN image datasets consisting of both discrete fields of view and entire biopsy sections imaged with a high channel dimension. Integration of these data reveal that CD4- T cell populations, comprised of CD8+, $\gamma\delta$ and double negative (CD4-CD8-δ-, DN) T cells, often organized into small cellular neighborhoods, are both associated with acute refractory disease and predict progression to renal failure. These and other findings indicate that in LN, systemic and *in situ* autoimmune pathogenic mechanisms are very different and that each might require specific targeted therapies.

Results

Accurate segmentation of immune cells in lupus nephritis kidney biopsies

To probe the relationship between TII and clinical outcome we used a well-characterized cohort of 55 biopsy-proven lupus nephritis patients with at least two years of follow up (**Supplementary Table 1**). Within this cohort, 19 patients progressed to end stage renal disease (ESRD+) while 36 did not (ESRD-). The ESRD+ and ESRD- groups did not differ in length of follow-up (**Supplementary Fig 1A**), duration of disease (**Supplementary Fig 1B**), or patient age (**Supplementary Fig 1C**). Forty-seven patients had moderate or severe TII distributed across both outcome groups. Based on previous studies[4], we hypothesized that differences in renal outcome would be related to differences in *in situ* adaptive immunity including both the frequencies and organization of principal cellular effectors. Therefore, we stained each biopsy for six markers, CD3, CD4, CD20, CD11c, BDCA2, and DAPI (nuclear marker) to characterize five classes of immune cells: CD3+CD4+ T cells, CD3+CD4- T cells, CD20+ B cells, BDCA2+ pDCs, and CD11c+ mDCs. Across the 55 biopsies, we captured all regions of interest (ROIs) with detectable CD3+ T cells, resulting in 865 ROIs. Image ROIs were 1024 x 1024 pixels, with a pixel size of 0.1058 μm. These data are referred to as the high resolution (HR) dataset.

Lupus nephritis is often characterized by chronic and intense inflammation in which it is difficult to accurately identify and segment specific cells using standard approaches due to the density of cells and the high levels of structured background signal[10,23]. Therefore, we trained deep convolutional neural networks (CNNs) to perform automatic cell detection, classification, and segmentation (collectively known as instance segmentation) on the HR dataset. To achieve optimal performance across all imaged cell classes, we split the five-class cell detection into two tasks: instance segmentation of lymphocytes and instance segmentation of DCs (**Fig 1A**). For each task, a separate instance of a region-based CNN architecture, Mask R-CNN, was independently trained (**Fig 1B**). Each Mask R-CNN was trained on 246 manually segmented images with a validation set of 65 manually segmented images used for hyperparameter tuning. On a test set of 30 images from patients unique to the training and validation data, the lymphocyte detection network had an F1-score of 0.75 and the DC

5

detection network of 0.57 while the overall F1-score for detection of all 5 cell classes was 0.74. Visual comparison of manual truth and predictions in individual ROIs revealed excellent concordance (**Fig. 1C**). By implementing deep CNNs, we achieve rapid and accurate whole-cell segmentation and classification.

Specific in situ immune cell densities associated with progression to renal failure.

Automatic cell segmentations were first used to describe and quantify the spatial distribution all five cell classes in the image dataset. Comparison of overall cell densities (total cells/ROI) in ESRD-patients and ESRD+ patients revealed no significant differences (**Fig 2A**). However, the total cell count per sample was higher in the ESRD+ cohort, reflecting larger overall areas of inflammation (**Fig 2B**). In contrast to overall cell density, there were apparent differences in the cellular constituents of inflammation between the two patient cohorts (**Fig 2C-G**). Surprisingly, ROIs from ESRD- patients had higher densities of B cells relative to ROIs from ESRD+ patients ($p=1.23 \times 10^{-7}$, **Fig 2C**). In contrast, ROIs from ESRD+ patients had increased densities of CD4- T cells ($p=3.40 \times 10^{-15}$, **Fig 2D**). There were no significant differences in the densities of CD4+ T cells, pDCs, or mDCs between patient cohorts (**Fig 2E-G**).

Although there were fewer ESRD+ patients, they had more ROIs captured per biopsy. To mitigate any effect from these cohort and individual class imbalances, we performed a bootstrapping analysis. The pools of ESRD+ and ESRD- ROIs were iteratively sampled with replacement 1000 times to produce samples of 200 ROIs from each group (ESRD+ and ESRD-). The distribution of mean cell densities between ESRD+ and ESRD+ patients revealed distinct, non-overlapping peaks for both B cells and CD4- T cells (**Fig. 2H-I**). In contrast, there was substantial overlap in the cell densities between ESRD+ and ESRD- patients for CD4+ T cells, pDCs and mDCs (**Fig. 2J-L**). The 95% confidence intervals of the difference in means between ESRD+ and ESRD- patients revealed for both B cells and CD4- T cells did not cross zero (**Supplementary Fig. 2A-B**). In contrast, the difference in means for the other cell types did cross zero (**Supplementary Fig. 2C-E**). These data indicate that the observed

differences in B cell and CD4- T cell densities between ESRD+ and ESRD- patients are robust. From these data we conclude that high B cell densities are associated with a good prognosis while high densities of CD4- T cells are associated with progression to renal failure.

When we examine these densities on the patient level, we observe that patients with high CD4- T cell densities, B cell densities tend to be low (**Fig 2M**). As indicated by point size, these tended to be ESRD+ patients with higher TI chronicity scores. The converse appeared true, as patients with higher B cell densities tended to have low TI chronicity scores and be ESRD-. These data suggest that lupus TII is associated with two or more distinct inflammatory states, each associated with a different prognosis.

Patients who present in renal failure have a skewed in situ inflammatory state

Within the ESRD+ group of patients was a small yet distinct cohort of five patients that either were in renal failure at the time of biopsy or progressed to renal failure within two weeks of biopsy collection. If these patients are treated as their own unique outcome group (ESRD current), differences in the density of specific cell classes becomes even more apparent (**Fig 3**)**.** There are progressively fewer B cells/ROI between ESRD-, ESRD+ and ESRD current groups respectively (**Fig. 3A**). The opposite trend is observed for CD4- T cell densities (**Fig 3B**). In contrast, there were no apparent differences in CD4+ T cells or pDCs in the ESRD current patients (**Fig. 3C-D**). Remarkably, there was a profound depletion of mDCs in the ESRD current cohort (**Fig. 3E**).

A three-group bootstrapping analysis was performed to assess any effect of class imbalance. This confirmed that ESRD current patients have the lowest mean density of B cells, followed by ESRD+, with ESRD- having the highest density of B cells (**Fig 3F**). Confidence intervals for the pairwise differences between these populations did not overlap with zero (**Supplementary Fig 3A**). An inverse, stepwise relationship was observed for CD4- T cells with progressively higher densities found in the ESRD+ and ESRD current relative to ESRD- cohorts (**Fig 3G, Supplementary Fig 3B**). ESRD-current patients were also well separated from the other two cohorts with respect to local mDC abundance (**Fig

3J, Supplementary Figure 3E). As expected, there were no differences between the three groups with respect to CD4+ T cells or pDCs (**Fig 3H-I, Supplementary Fig 3C-D).** These findings indicate that patients presenting in renal failure have a skewed inflammatory state with abundant CD4- T cells, relatively few B cells and a depletion of mDCs.

It is possible that the inflammatory phenotype observed in ESRD current patients was not a primary state but arose as a secondary consequence of renal damage and scarring. However, two patients in the ESRD current cohort (**Supplementary Table 1**, patients 51 and 55) presented with very high activity indices and relatively low TI chronicity scores (2 out of a possible 6 points)[26]. These observations suggest that the skewed inflammatory phenotype observed in ESRD current patients can precede severe renal injury.

Specific cellular neighborhoods associated with progressive and refractory renal disease.

We next explored the relative *in situ* spatial relationships between the different immune cell classes. First, for every cell in the dataset, we identified the nearest neighbor using centroid to centroid distances. CD4+ and CD4- T cells were significantly more likely to have a B cell as their nearest neighbor in ESRD- biopsies (p=1.00×10^{-36} and p=6.23×10^{-19}, respectively) (**Fig 4A**). In contrast, CD4+ T cells and B cells were significantly more likely to have a CD4- T cell nearest neighbor in ESRD+ biopsies (p=7.53×10^{-29} and p=6.35×10^{-9}, respectively) (**Fig 4B**). Additionally, both B cells and CD4- T cells showed a strong propensity for co-localization with cells of the same type (p=1.09×10^{-8} and p=1.75×10^{-9}, respectively).

Higher order local cellular organization was then probed by grouping cells into spatially discrete neighborhoods. DBSCAN, a density-based clustering algorithm[27], was implemented to group cells into discrete neighborhoods defined by a maximum intercellular centroid-centroid distance. Variation in this maximum distance between 50 and 150 pixels resulted in a range of neighborhood sizes varying between those that contained just a few cells (50 pixels) to those that encompassed large areas of inflammation (150 pixels) (**Fig 4C, Supplementary Fig 4A**). A maximum distance of 100 pixels (~10.6

8

µm) was selected, as this distance approximates a cell body and appeared to resolve observable regional behavior across the dataset.

Using this 100-pixel cutoff and a minimum neighborhood size of two, DBSCAN detected 4022 cell neighborhoods in the dataset. Each neighborhood was quantitatively characterized by a set of 24 features including cell type frequency, cell type proportion, ratios of cell types, average cell shape features, and the overall area of the neighborhood (**Supplementary Fig 4B**). K-means clustering was then applied to define classes of neighborhoods. The neighborhoods were split into six classes, as determined ideal by bootstrapping cluster descriptors including the within cluster sum of squares (WCSS) and the delta WCSS (**Supplementary Fig 4C-D**). The test score from a leave-one-out t-test approach was used to determine which features or combination of features best distinguished the six neighborhood groups (**Fig 4D**). The most distinctive feature(s) for each group was used to describe the cell neighborhoods as follows: 1) B cell enriched cluster, 2) CD4- T cell enriched cluster, 3) Large, lymphocyte enriched cluster, 4) CD4+ T cell enriched cluster, 5) mDC enriched cluster, and 6) pDC enriched cluster (**Fig 4E**).

Tertiary lymphoid structures (TLSs) have been previously identified in the context of lupus nephritis[13]. Although we cannot explicitly define TLSs in this dataset, we hypothesized that the large, lymphocyte enriched neighborhoods might approximate TLSs. For example, we noted that within this group, 28.6% of the cells were B cells and 48.3% were CD4+ T cells. Furthermore, 96.1% of these neighborhoods met the following criteria: 1) contained at least 20 cells, 2) both B cells and CD4+ T cells were represented in the neighborhood and 3) at least 50% of all cells were B cells and/or CD4+ T cells. Therefore, the vast majority of large, lymphocyte enriched neighborhoods, have features consistent with TLSs.

We then examined how these six classes of neighborhoods were distributed between the ESRD- and ESRD+ patients. After normalizing for the number of ROIs captured for each patient, ESRD- and ESRD+ patients had no difference in their total neighborhood count per ROI (**Fig 4F**). However, ESRD+ patients had significantly higher prevalence of CD4- T cell enriched neighborhoods relative to the

ESRD- patients (p = 0.043) (**Fig 4G**). The per ROI prevalence of the other classes of neighborhoods did not correlate with renal outcome (**Supplementary Fig 5A-E**). We next examined if the CD4-neighborhoods differed between the ESRD-, ESRD+ and ESRD current patient groups (**Fig 4H**). ESRD+ and ESRD current patients had a statistically higher prevalence of neighborhoods from the CD4- cluster than ESRD- patients (p=0.03, p=0.009, respectively). These data demonstrate that, on a per patient basis, the prevalence of small, CD4- T cell enriched neighborhoods demonstrates the strongest association with progressive renal disease.

Cell detection and segmentation in highly multiplexed, full-biopsy images

To better characterize *in situ* lymphocyte populations, we performed highly multiplexed confocal microscopy on a separate dataset of 18 lupus nephritis biopsies. In this highly multiplexed (HMP) dataset, we interrogated a set of nine markers (CD3, CD4, CD8, ICOS, PD1, FoxP3, CD20, CD138, and DAPI). This highly multiplexed panel was obtained using four color confocal microscopy and iterative stripping and reprobing[28]. In addition, we imaged full biopsy sections rather than capturing isolated ROIs thereby facilitating a more complete and unbiased spatial analysis.

Full biopsy images for all stains were aligned with the DAPI channel (**Fig 5A**). Two new instances of Mask R-CNN were trained to perform single-marker and dual-marker instance segmentation (**Fig 5B**). Briefly, ROIs from the HR dataset (pixel size = 0.1058 µm) were broken up into 512 x 512 pixel tiles to pre-train each Mask R-CNN. Each network was then fine-tuned using small sets of manually segmented 512 x 512 pixel tiles from the HMP dataset (pixel size = 0.221 µm). The single-marker Mask R-CNN was used to predict B cells (CD20+) and plasma cells (CD138+), while the dual-marker Mask R-CNN was used to predict single positive and double positive T cells. The three main classes of T cells (CD4, CD8, and DN) were determined by combining predictions from a CD3/CD4/DAPI image stack with predictions from a CD3/CD8/DAPI image stack at the same location in the tissue (**Fig 5C**). The dual-marker Mask R-CNN was used to generate cell predictions on CD3/ICOS/DAPI and CD3/PD1/DAPI images. The resulting single-positive (CD3+ICOS- or CD3+PD1-) and double-positive

(CD3+ICOS+ or CD3+PD1+) predictions were to define ICOS and PD1 expression for every putative T cell in the dataset. As FoxP3 is nuclear, these images were binarized by thresholding individual image tiles. T cell predictions with > 25% overlap with this binary mask were determined to be FoxP3+.

CD4- T cells contain CD8, γδ and other DN T cell populations

T cells comprised over 65% of all predicted lymphocytes in the HMP dataset (**Fig 5D**). Plasma cells were the second most abundant class in the dataset, comprising ~28% of all detected lymphocytes. B cells were least prevalent at only ~6% of detected lymphocytes. CD4+ T cells were the most abundant cell class across all five main classes, making up 35% of all lymphocytes, and over 50% of all detected cells (**Fig 5E**). Surprisingly, CD8 T cells were only slightly more abundant than double negative (CD4-CD8-, DN) T cells, comprising ~17% of all lymphocytes and ~26% of all T cells.

To further characterize these DN T cells, we interrogated public scRNA-Seq data of immune cells infiltrating the kidney of lupus nephritis patients[18]. We identified naïve T and CTL clusters in intrarenal immune cells by unsupervised clustering and canonical marker expression (**Fig 6A**). Within these T cell clusters, 21% were DN, as measured by the UMI of *CD4*, *CD8A*, and *CD8B* (**Supplementary Fig 6A**). Several T cell subtypes do not express CD4 nor CD8 including natural killer (NK) T cells and γδ T cells. Indeed, there was a small increase in *CD3D* in cells assigned to the NK cell class, suggesting a NKT phenotype. However, there was not a substantial enrichment for NKT cell markers in the DN subset (**Supplementary Fig 6B**).

Next, we compared TCRα and δ chain expression (*TRAC* and *TRDC*). Some cells were apparently positive for both *TRAC* and *TRDC*, likely due to sequence homology between these genes (**Fig 6B**). However, *TRAC*- cells and *TRDC*+ cells were both enriched in DN population (**Fig 6C**). These results suggest that a portion of the DN T cells observed in lupus nephritis are γδ T cells. To examine this possibility further, we stained eight lupus nephritis biopsies with antibodies specific for CD3, CD4, CD8, TCRδ, and imaged 281 ROIs (**Fig 6D**). In a given biopsy, 51.4% ± 21.3% of DN T cells were

11

positive for TCRδ. These findings indicate a substantial fraction of T cells in lupus nephritis do not detectably express CD4 nor CD8, and approximately half of these DN T cells are $\gamma\delta$ T cells.

In situ distributions of exhausted, regulatory and helper T cell populations

We then examined the distributions of ICOS, PD-1 and FoxP3 in the T cell subsets. Roughly 30% of CD8+ T cells in the HMP dataset are PD1 positive (**Supplementary Fig 7A**) suggesting an exhausted phenotype. Approximately 25% of CD8+ T cells were "exhausted" by the definition of PD1+ICOS-FoxP3-[29]. This is coherent with observations from murine lupus models in which exhausted tissue-infiltrating CD8+ T cells are relatively common[30]. In contrast, human lupus renal scRNA-Seq data suggests that CD8+ T cell exhaustion is infrequent[2].

A surprisingly small percentage (5.41%) of CD4+ T cells were FoxP3 positive, while fewer still were also PD1-ICOS-, suggesting that Tregs comprise only about 2.5% of CD4+ T cells (**Supplementary Fig 7B**). In contrast, even fewer CD8+ T cells (1.3%) or DN T cells (0.88%) expressed FoxP3 (**Supplementary Fig 7A,C**). Therefore, very few of the tissue-infiltrating CD4+ T cells in lupus nephritis are potentially Tregs.

We additionally identified T follicular helper-like (Tfh) cells based on the combination of PD1 and ICOS expression by CD4+ T cells[31,32]. 5.05% of the CD4+ T cell compartment were PD1+ICOS+FoxP3-. However, given that previous investigations have consistently associated PD1 expression with Tfh-like cells, but not necessarily ICOS, we decided to use a less stringent definition of PD1+ICOS+/-FoxP3- to identify this cell subset in our data. This phenotype was associated with roughly 30% of the CD4+ T cells (**Supplementary Fig 7B**). Though it should be noted that PD1+ICOS-FoxP3-CD4+ T cells could alternatively be interpreted as exhausted, we chose to use the more expansive definition in our subsequent analysis.

Organization of inflammation across whole biopsies

We next probed the potential interacting partners of Tfh, Treg, and Tex cells by identifying the class of their nearest neighbors. Most Tregs are closest to other Tregs and other non-specific CD4+ T cells (**Supplementary Fig 7D**). In contrast to the expectation that Tfh would primarily be in close proximity with CD20+ B cells, Tfh had other CD4+ T cells as their most frequent neighbor, followed by other Tfh (**Supplementary Fig 7E**). Exhausted CD8+ T cells were most frequently found near other exhausted CD8+ T cells, followed by CD4+ T cells and CD8+ T cells (**Supplementary Fig 7F**). Overall, these data demonstrate that across biopsies there is a tendency for the clustering of similar cells together.

Cell neighborhoods in the HMP dataset were then defined using DBSCAN with a distance cutoff of 50 pixels, or roughly 10 µm. Most of the neighborhoods detected in the dataset were small (**Fig 7A**). However, without the constraint of discrete fields of view, we were able to capture neighborhoods of up to 273 cells. In contrast, the largest neighborhood captured in the HR dataset (which was restricted to a to ~1.2×10^4 µm^2 of tissue), contained only 147 cells. Given the association of CD4- T cell enriched neighborhoods with ESRD+ patients in the HR data, we investigated similar CD4- neighborhoods in the HMP data. We classified CD4- neighborhoods as those that had 1) less than 20 cells and 2) 25% of their cells as either CD8 T cells or DN T cells, as these criteria captured the CD4- neighborhoods observed in the HR data (**Fig 7B**). A strong majority of the cells in these neighborhoods are CD4- T cells, including 26% DN T cells and 34.2% CD8+ T cells (**Fig 7C**). There was a weak negative correlation (R=-0.35) between the number of DN T cells and CD8+ T cells in these neighborhoods, suggesting that DN and CD8+ T cells are not proportionally represented in a given neighborhood.

Large B-T neighborhoods were defined by the set of criteria (described above) that captured most of the large, lymphocyte-rich neighborhoods in the HR data. Of nearly 14,000 neighborhoods in the HMP dataset, 111 met these criteria (representative clusters in **Fig 7D)**. Within these B-T neighborhoods, a vast majority of the lymphocytes were T cells, followed by similar proportions of B cells and plasma cells (**Fig 7E**). Tfh cells made up 36% of CD4+ T cells in B-T neighborhoods (**Fig 7F)**

13

which was a significant enrichment compared to non-B-T neighborhoods (p = 1.9x10^{-6}, Mann-Whitney) (**Fig 7G**). As observed across whole biopsies, within these B-T neighborhoods, homotypic proximity predominated. B cells were located near other B cells, followed by plasma cells and CD4+ T cells (**Fig 7H**). Tfh cells in these neighborhoods were most often near other Tfh cells, while overall Tfh were near unspecified CD4+ T cells (**Fig 7I, Supplementary Fig 7E**). Putative exhausted T cells tended to be close to each other, followed by unassigned CD4+ T cells (**Supplementary Fig 7F**). Unassigned CD4+ T cells in B-T neighborhoods were also most likely to be found near other CD4+ T cells, followed by Tfh cells (**Fig 7J**).

Cellular neighborhoods in both datasets were defined by the approximate size of a cell body and excluded longer-range interactions. A simple visual inspection reveals that neighborhoods are rarely isolated from each other (**Fig 8A**). To investigate potential higher order organization, we calculated inter-neighborhood distances. The average nearest-neighborhood distance was 158.5 pixels, roughly 35 μm. The distribution of minimum distances to the nearest neighborhood is heavily skewed towards short distances (**Fig 8B**), suggesting that most cell neighborhoods exist within large inflammatory structures which we refer to as "cities". Interestingly, the largest neighborhoods were typically near other cellular neighborhoods, while small cellular neighborhoods had much more variability in their nearest-neighborhood distances (**Fig 8C**).

Discussion

Canonically, lupus nephritis is thought of as arising from a systemic break in B cell tolerance leading to glomerular antibody deposition and inflammation. This model, supported by large bodies of evidence in both humans and mice[8,33], has led to clinical trials targeting B cells and Tfh cells[34-40]. However, these efforts have yielded either incremental or negative improvement over the standard of care. By quantifying cellular organization within conventional and highly multiplexed confocal microscopy images using deep learning algorithms, we demonstrate that high regional B cell density is associated with a good prognosis. Rather, it is CD4- T cell populations, including CD8+, $\gamma\delta$, and other DN T cells, that are associated with refractory disease and progression to renal failure.

The CD4- population was surprisingly heterogeneous. As expected, CD8 expressing cells were common. However, over 40% of the CD4- cells did not express CD8. Of these approximately 50% expressed the $\gamma\delta$ TCR. Re-examination of the AMP data confirmed the presence of intrarenal $\gamma\delta$ T cells within the DN T cells. The DN T cells described in LN have been theorized to arise from CD8+ T cells that downregulate CD8 expression[41,42]. To our knowledge, this is the first study to quantify DN T cell prevalence in LN and to differentiate true DN from $\gamma\delta$ T cells.

It remains to be determined whether one of these populations is clearly associated with progression to renal failure or if these populations share pathogenic roles. Certainly, both CD8 and $\gamma\delta$ T cells can be cytolytic and might provide complementary recognition of different classes of autoantigens[43-46]. The function of DN T cells is not known. However, if they are derived from CD8 T cells they might also retain cytolytic activity[41]. It is clear that the heterogeneity in the DN T cell or CD8+ populations must be resolved before accurately assigning pathogenicity and identifying the populations most closely linked with ESRD.

In addition to yielding information on cell frequencies in tissue, our analytic pipelines provided the precise positions of all cells assayed in the biopsy. This allowed us to define cellular neighborhoods and extract quantitative features including neighborhood size, shape and cell constituency. Unsupervised clustering revealed that small neighborhoods of CD4- T cells were associated with

15

progression to ESRD. Even within our small cohort, CD4- T cell neighborhoods were associated with renal failure in individual patients.

Our data identify CD4- T cells, including CD8+, $\gamma\delta$, and DN T cells as potentially important therapeutic targets. This association was particularly striking in patients that presented in renal failure. Two patients who initially presented with renal failure had high densities of CD4- T cells and relatively low chronicity scores, suggesting that infiltrating CD4- T cells can precede substantial renal damage. These data suggest that patients exhibit distinct, prognostically meaningful, intra-renal inflammatory trajectories.

Unfortunately, in contrast to the B cell:Tfh axis, we have limited therapeutic options that specifically target these T cell populations. One of the few classes available are calcineurin inhibitors (CNIs). The recent success of the CNI voclosporin in treating some patients with lupus nephritis is promising[47]. We propose that stratifying patients by the constituency and organization of their renal inflammation might identify those most likely to benefit from the addition of T cell targeting therapies such as voclosporin.

Collections of B cells were surprisingly associated with a good renal outcome. It is possible that B cells and subsequent local antibody secretion are somewhat benign compared to other pathological processes. Alternatively, conventional therapies might be relatively effective against B cells and plasma cells. Therefore, B cell density in a diagnostic biopsy could indicate patient response to these therapies. Indeed, most of our patients were treated with high-dose steroids and induced with cytotoxic therapies, most often mycophenolate. These therapies have been demonstrated to deplete B cells and plasma cells[48,49].

Large neighborhoods of cells were enriched in both B cells and CD4 T cells, which were found to include a higher prevalence of Tfh cells than other neighborhoods. These neighborhoods have similar features to the T:B aggregates described previously[13]. However, our HMP image analysis indicated that these structures are more complex containing other cell types including other CD4+ T cell and PC populations. These findings cohere with previous studies that suggest an underlying

16

architecture to these large neighborhoods[11]. In addition, we found that large neighborhoods tended to aggregate together into cities. Further work will be needed to understand the rules by which these cities organize, and the underlying biological processes governing their organization.

Interestingly, pDC prevalence was not associated with renal outcome in our HR dataset. As sources of IFNα, they have been postulated to play a central role in disease pathogenesis[50-53]. However, the outcomes of clinical trials of anti-IFNα antibodies in lupus have been modest[54,55]. In contrast to pDCs, mDCs were depleted in those patients that presented in renal failure. While seemingly counterintuitive, tubulointerstitial DCs can retain an immature phenotype in lupus nephritis[56]. Therefore, they might have a role in organ tolerance even in the context of severe inflammation. It should be noted that the interstitial mDCs we quantified appeared different than the periglomerular inflammatory mDCs that have been recently described in lupus nephritis [57].

With deep learning and other artificial intelligence algorithms, we achieved robust and accurate cell detection across multiple lupus nephritis image datasets, thereby facilitating a detailed, accurate spatial analysis of *in situ* immunity in lupus nephritis samples. Several computer vision methods were implemented to establish an analytical pipeline that addressed experimental, biological, and technical limitations. CNNs trained for instance segmentation detected and classified several immune cell classes with high fidelity not only in sparsely populated images, but also in densely packed images. We also trained and implemented CNNs for rapid and robust image and object filtering to optimize immune cell calling in full-biopsy sections. This included a network trained to discriminate between image tiles containing positive cell signal and erroneous tissue autofluorescence. We also trained a network to segment tubules in order to reject false-positive plasma cell predictions. By combining these CNNs with conventional thresholding and image registration techniques, we automatically mapped several immune cell classes to full-biopsy sections enabling a robust spatial analysis of *in situ* autoimmunity.

Using artificial intelligence to quantify immune cell populations in human tissue, we extracted rich, non-biased, spatio-cellular data that allowed identification of unexpected pathogenic mechanisms. Even in a relatively small longitudinal cohort, we were able to resolve patient heterogeneity to identify

17

putative pathogenic processes. Remarkably, specific cell densities provided powerful insights into disease pathogenesis. Understanding how these populations were organized into neighborhoods provided predictive power in individual patients. Furthermore, this work revealed fundamental insights to the structural organization of inflammation that began to identify organizing principles. Further studies of the complexity, heterogeneity and organization of *in situ* inflammation will yield a better, more quantitative understanding of human autoimmunity. Such knowledge is critical for interpreting and applying the wealth of knowledge we have gained from animal models. It is also likely to identify both new therapeutic targets and those patients in which specific strategies are likely to be beneficial.

Materials and Methods

Sample staining and image acquisition: High-resolution dataset

Formalin-fixed paraffin-embedded (FFPE) kidney biopsies from 55 lupus nephritis patients with at least two years of clinical follow-up were obtained from the University of Chicago Human Tissue Resource Center. FFPE sections were de-paraffinized and treated with a citric acid buffer (pH 6.0) for antigen retrieval and blocked with serum prior to antibody staining. Samples were stained with indicated specific antibodies (**Supplementary Table 2**). Stained samples were imaged on a Leica SP8 laser scanning confocal microscope at 63x magnification. Images were collected wherever CD3 signal was present in a biopsy. Collected images were 1024 x 1024 pixels x 6 channels with a 0.1058 μm pixel size.

Staining and image acquisition: Highly multiplexed dataset

Samples were stained using a strip and reprobe procedure in which 5 μm thick sections of FFPE biopsy sections were iteratively stained according to a procedure outlined by[28]. Sections were deparaffinized and stained with a combination of primary antibodies and secondary antibodies conjugated with AlexaFluor 488, 546, and 647 fluorophores (**Supplementary Table 2**). DAPI was also included in every iteration of staining. For each round of staining, samples were imaged using a Caliber ID RS-G4 large-format confocal microscope at a magnification of 63x, resulting in a pixel size of 221 nm. After each round of imaging, samples were stripped as described[28]. Samples were then re-probed with a new set of primary and secondary antibodies and re-imaged until the full marker panel had been imaged.

Staining and image acquisition: $\gamma\delta$ T cells

Eight lupus nephritis kidney biopsies were stained for CD3, CD4, CD8, TCRδ, and DAPI. Inflamed regions were imaged on the Leica Stellaris 8 confocal microscope, with 40x magnification and a pixel size of 0.225 um. 281 ROIs (35±19 per sample) 1024x1024 ROIs were obtained, and then post

processed with background subtraction, de-speckling and contrast adjustment using ImageJ. Cells in these images were quantified by manual count.

Automatic cell detection and segmentation: High resolution dataset

Two instances of a Mask R-CNN architecture[58] were trained to detect and segment cells in this dataset. One instance was trained to explicitly detect three classes of lymphocytes (B cells, CD3+CD4- T cells, and CD3+CD4+ T cells). A second instance was trained to detect two classes of DCs (pDCs and mDCs). Mask R-CNN is a region-based convolutional neural network (CNN) composed of a feature pyramid network (FPN), region proposal network (RPN), then simultaneous object classification, bounding box regression, and object segmentation. For this work, a ResNet-101 was used as a backbone for the FPN. Networks were trained with a learning rate of 0.01. Training, validation, and testing data were generated by a single expert manually segmenting all five cell classes in an image. All manually segmented images from a given patient were relegated to either the training set (273 images, 80%), validation set (34 images, 10%), or test set (35 images, 10%). Training progress was monitored using Tensorboard and training was stopped after cell recall stopped improving for all classes. Precision (Eq.1), recall (Eq. 2), and F1-score (Eq. 3) were used to evaluate network performance. All computation for the HR dataset was performed using resources at the University of Chicago Research Computing Center. Each instance of Mask R-CNN was trained on a single GPU compute node containing four Nvidia GPUs with 12GB memory per card, 28 Intel E5-2680v4 CPUs at 2.4 GHz, and 64 GB of system memory. A batch size of 4 images was used for training, distributed across the four GPU cards. Networks were trained to the point at which the recall for all cell classes stopped increasing.

$$Precision = \frac{true\ positives}{true\ positives + false\ positives}, \qquad (1)$$

$$Recall = \frac{true\ positives}{true\ positives + false\ negatives}, \qquad (2)$$

$$F1\ score = \frac{2*Precision*Recall}{Precision+Recall}, \qquad (3)$$

20

Automatic cell detection and segmentation: Highly multiplexed dataset

First, the Caliber ID microscope output images in the form of image strips were stitched together using cross-correlation of image patches at the strip boundaries. These single-channel composites were then aligned with the DAPI channel from the first round of imaging, again through cross-correlation of image windows. Composites were then broken into 512 x 512 pixel image tiles. All DAPI tiles were passed through a simple image intensity filter to determine if tissue was present at a given location. All tiles at a given location were filtered out of proceeding analyses if the DAPI filter revealed no tissue at that location. This resulted in over unique 18,000 tile locations, with each location containing nine unique stains.

Some of the resulting tissue-containing tiles did not contain immune cells. Furthermore, the tissue autofluorescence generates false positive cell proposals. Therefore, all locations with tissue present were again filtered for lymphocyte presence based on positive CD3 and/or positive CD20 signal. This was accomplished by training an 18-layer CNN, similar to a VGG19 architecture[59], to classify CD3 and CD20 image tiles as inflamed or uninflamed. 536 CD3 and CD20 tiles from 18 patients were manually classified as either inflamed or uninflamed by a single expert for training (354 images, 66%), validation (91 images, 17%), and testing (91 images, 17%) sets. All images from a given patient sample were constrained to a single set to avoid data leakage. The network was trained with a learning rate of 9e-5, using dropout and data augmentation of random image flips and rotations. Training was stopped once the validation accuracy had not improved in 10 epochs. The trained network had a receiver operator characteristic (ROC) area under the curve (AUC) of 0.991. Only image tiles at locations corresponding to CD3 and/or CD20 positive signal (inflamed) proceeded to cell segmentation. Instance segmentation of cells was split into two tasks: instance segmentation of T cells (also referred to as dual-marker detection) and instance segmentation of B cells (also referred to as single-marker detection). Instance segmentation performance was evaluated using precision (Eq. 1), recall (Eq. 2), and F1-score (Eq. 3).

T cell segmentation: An instance of Mask R-CNN was trained to segment single positive (CD3+CD4-) and double positive (CD3+CD4+) T cells in the high-resolution T cell image stacks described above. This trained network was fine-tuned with a small set of 211 T cell image stacks from the highly multiplexed dataset. The highly multiplexed fine-tuning image sets contained DAPI in combination with CD3/CD4, CD3/CD8, or CD3/ICOS channels. This fine-tuning set was split into training (169 images, 80%), validation (21 images, 10%), and testing (21 images, 10%) sets, with all images from a given patient confined to a specific set. For fine-tuning, the weights were permitted to adjust for all convolutional, max-pooling, and fully connected layers of the Mask R-CNN instance pre-trained on high-resolution T cell images. The fine-tuned T cell network was used to make predictions for CD3/CD4, CD3/CD8, CD3/ICOS, and CD3/PD1 images. The trained dual-marker network had an average F1-score of 0.85 on all single-positive cell predictions (i.e. CD3+CD4- and CD3+CD8-) and an average F1-score of 0.92 on all double-positive cell predictions (i.e. CD3+CD4+ and CD3+CD8+).

B cell segmentation: An instance of Mask R-CNN was trained to segment B cells in the high-resolution B cell image stacks described above. This trained network was fine-tuned with a set of 79 B cell image stacks from the HMP dataset. This fine-tuning set was split into training (63 images, 80%), validation (8 images, 10%), and testing (8 images, 10%) sets, with all images from a given patient confined to a specific set. For fine-tuning, the weights were permitted to be adjusted for all convolutional, max-pooling, and fully connected layers of the Mask R-CNN instance pre-trained on HR B cell images. The fine-tuned B cell network was used to make predictions for B cell (CD20) and plasma cell images (CD138). The trained single-marker network had and average F1-score of 0.87.

Tubule segmentation

An instance of Mask R-CNN was trained to segment tubular structures in the HMP dataset, encompassing both renal tubules and blood vessels. 300 DAPI tiles from 18 patients (512 x 512 pixels) were manually annotated by a single expert. Manually segmented images were separated into training, validation, and testing sets as follows: 240 images in the training set (80%), 30 images in the validation

22

set (10%), and 30 images in the test set (10%). Data augmentation consisted of random horizontal and vertical flips and rotations. Performance of the tubule segmentation network was assessed at the pixel level, with the trained network yielding a recall (Eq. 2) of 0.74 and an average precision (Eq. 1) of 0.79 on the test set of tubule images.

All pre-processing and computation associated with instance segmentation in the HMP dataset was performed on the MEL computational server in the Radiomics and Machine Learning Facility at the University of Chicago. MEL contains 256 Xeon Gold 6130 CPU cores, 3TB of DDR4 ECC RAM memory, 24TB of NVMe SSD storage, and 16 nVidia Tesla V100 32GB GPU accelerators.

Defining cell neighborhoods through density-based clustering

Cells in both datasets were assigned to clusters using the sklearn (version 0.23.2) implementation of Density Based Spatial Clustering of Applications with Noise (DBSCAN)[27], using an epsilon of roughly 10 μm, corresponding to 100 pixels in the HR dataset and 50 pixels in the HMP dataset. Minimum cluster size was defined as two points (cells). Neighborhoods were generated based on coordinates of the cellular centroids within the full composite. Twenty-four features that capture cellular constituency as well as cell and neighborhood shape, were extracted for each cluster, and K-means clustering was then applied to define classes of neighborhoods. The neighborhoods were split into six classes as determined ideal by bootstrapping cluster descriptors including the within cluster sum of squares (WCSS) and the delta WCSS. The types were characterized using a leave-one-out t test to identify which features of each type of neighborhood distinguished it from the other neighborhoods. In this procedure, the current cluster of reference was treated as the alternative group, all the remaining clusters were then binned together as the reference group, then a t-test for was applied for all features used to describe the neighborhoods.

Area calculation

The total area of tissue in each sample was calculated by analyzing the DAPI composite in the following way: 1) a threshold pixel intensity of 5 was applied to binarize the image; 2) the skimage.morphology (version 0.17.2) functions "area_closing" (area_threshold=5000), "remove_small_holes" (area_threshold=5000), "remove_small_objects" (min_size=100), and "binary dilation" were applied to the image in that order to fill in small areas of tissue that did not contain nuclei; 3) the number of positive pixels was then calculated and converted to units of um^2 using 0.0488 $um^2/pixel^2$ as the conversion factor. The number of cells per unit area were calculated by dividing the cellular content of the full composite by this calculated area.

Spatial Analyses

All other spatial analyses were performed in the programming language Python (3.7.9). The following packages were utilized for analysis: pandas (1.2.2), numpy (1.19.2), sklearn (0.23.2), scipy (1.6.1), and tifffile (2021.1.14). Plotting was performed with matplotlib (3.3.2) and seaborn (0.11.1). The nearest neighbors calculation was performed by iterating through every cell in the dataset and identifying the class of the segmented cell that was closest to it based on centroid to centroid distance

In the HMP dataset, coordinates of the cells in the tiles were adjusted to a composite-level coordinate system by shifting the tile-level coordinates based on the location of the tile in the composite. All subsequent calculations around the distribution of cells in tissue were based on these composite-level locations. In order to evaluate the distances between neighborhoods, a bounding box was drawn around each cellular neighborhood, and the coordinates of the center of the box was used as an approximate neighborhood centroid. The centroid-centroid distance between each neighborhood and the neighborhood closest to it was identified.

RNA sequencing analysis

Single-cell RNA-seq data for human lupus nephritis tissue were obtained from the ImmPort repository (accession code SDY997, "SDY997_EXP15176_celseq_matrix_ru10_molecules.tsv" raw

24

data file). Quality control was performed according to the original paper[18], such that cells were removed from the analysis if they expressed <1,000 or >5,000 genes, or if more than 25% of the total unique molecular identifiers (UMI) mapped to mitochondrial genes. Gene expression values were normalized to library size (UMI count per million) and scaled by log2. Clustering implemented in Seurat 3.2.2 and canonical marker expression were used to identify cellular subsets. T cells were analyzed if they were assigned to the "Naïve T" or "CTL" clusters. T cells were categorized based on *CD4*, *CD8A,* and *CD8B* expression. Cells were categorized as "CD4" when they had detectable expression of *CD4* transcripts but no *CD8A* or *CD8B.* They were instead categorized as "CD8", when they had detectable *CD8A* and/or *CD8B* with no *CD4* transcripts. Cells were categorized as DP (double-positive) or DN (double-negative) when they had both/neither *CD4* and/nor *CD8A/B*. t-SNE was performed by Rtsne (0.15). Plots were generated by ggplot2 (3.3.2) and ggridges (0.5.2).

References

1   Tan, E. M. & Kunkel, H. G. Characteristics of a soluble nuclear antigen precipitation with sera of patients with systemic lupus erythematosus. *J Immunol* **96**, 464-471 (1966).
2   Dubois, E. L. *Lupus Erythematosus - Second Edition.* (W.B Saunders 1974).
3   Markowitz, G., D'Agati VD. Classification of lupus nephritis. *Curr Opin Nephrol Hypertens* **18**, 220-225 (2009).
4   Hsieh, C. *et al.* Predicting outcomes of lupus nephritis with tubulointerstitial inflammation and scarring. *Arthritis care & research* **63**, 865-874, doi:10.1002/acr.20441 (2011).
5   Esdaile, J. M., Levinton, C., Federgreen, W., Hayslett, J. P. & Kashgarian, M. The clinical and renal biopsy predictors of long-term outcome in lupus nephritis: a study of 87 patients and review of the literature. *Q J Med* **72**, 779-833 (1989).
6   Yu, F. *et al.* Tubulointerstitial lesions of patients with lupus nephritis classified by the 2003 international society of nephrology and renal pathology society system. *Kid Int* **77**, 820-829 (2010).
7   Schwartz, M., Fennell, J. S. & Lewis, E. J. Pathologic changes in the renal tubule in systemic lupus erythematosus. *Hum Pathol* **13**, 534-547 (1982).
8   Chang, A., Clark, M. R. & Ko, K. Cellular aspects of the pathogenesis of lupus nephritis. *Current opinion in rheumatology* **33**, 197-204, doi:10.1097/bor.0000000000000777 (2021).
9   Kinloch, A. J. *et al.* Anti-vimentin antibodies: a unique antibody class associated with therapy-resistant lupus nephritis. *Lupus* **29**, 569-577, doi:10.1177/0961203320913606 (2020).
10   Liarski, V. *et al.* Quantifying in situ adaptive immune cell cognate interactions in humans. *Nature Immunology* **20**, 503-513 (2019).
11   Liarski, V. *et al.* Quantitative cell distance mapping in human nephritis reveals organization of in situ adaptive immune responses. *Sci Trans Med* **6(230):230ra46** (2014).
12   Kinloch, A. J. *et al.* Vimentin is a dominant target of in situ humoral immunity in human lupus tubulointerstitial nephritis. *Arthritis Rheumatol* **66**, 3359-3370, doi:10.1002/art.38888 (2014).
13   Chang, A. *et al.* In situ B cell-mediated immune responses and tubulointerstitial inflammation in human lupus nephritis. *J Immunol* **186**, 1849-1860, doi:10.4049/jimmunol.1001983 (2011).
14   Adalid-Peralta, L. *et al.* Leukocytes and the kidney contribute to interstitial inflammation in lupus nephritis. *Kid Int* **73**, 172-180 (2008).
15   Clark, M. R., Trotter, K. & Chang, A. The pathogenesis and therapeutic implications of tubulointerstitial inflammation in human lupus nephritis. *Seminars in nephrology* **35**, 455-464, doi:10.1016/j.semnephrol.2015.08.007 (2015).
16   Odegard, J. M. *et al.* ICOS controls effector function but not trafficking receptor expression of kidney-infiltrating effector T cells in murine lupus. *J Immunol* **182**, 4076-4084 (2009).
17   Sekine, H., Watanabe, H. & Gilkeson, G. S. Enrichment of anti-glomerular antigen antibody-producing cells in the kidneys of MRL/MpJ-Fas(lpr) mice. *J Immunol* **172**, 3913-3921 (2004).
18   Arazi, A. *et al.* The immune cell landscape in kidneys of patients with lupus nephritis. *Nat Immunol* **20**, 902-914, doi:10.1038/s41590-019-0398-x (2019).
19   Der, E. *et al.* Tubular cell and keratinocyte single-cell transcriptomics applied to lupus nephritis reveal type I IFN and fibrosis relevant pathways. *Nat Immunol* **20**, 915-927, doi:10.1038/s41590-019-0386-1 (2019).
20   Ko, K. *et al.* BCL-2 as a therapeutic target in human tubulointerstitial inflammation. *Arth Rheum* **68**, 2740-2751 (2016).
21   Amgad, M. *et al.* Joint Region and Nucleus Segmentation for Characterization of Tumor Infiltrating Lymphocytes in Breast Cancer. *Proc SPIE Int Soc Opt Eng* **10956**, doi:10.1117/12.2512892 (2019).
22   Durkee, M. S., Abraham, R., Clark, M. R. & Giger, M. L. Artificial Intelligence and Cellular Segmentation in Tissue Microscopy Images. *Am J Pathol*, doi:10.1016/j.ajpath.2021.05.022 (2021).
23   Durkee, M. S. *et al.* Quantifying the effects of biopsy fixation and staining panel design on automatic instance segmentation of immune cells in human lupus nephritis. *J Biomedical Optics* **26**, https://doi.org/10.1117/1111.JBO.1126.1112.022910 (2021).
24   Madabhushi, A. & Lee, G. Image analysis and machine learning in digital pathology: Challenges and opportunities. *Med Image Anal* **33**, 170-175, doi:10.1016/j.media.2016.06.037 (2016).
25   Schürch, C. M. *et al.* Coordinated Cellular Neighborhoods Orchestrate Antitumoral Immunity at the Colorectal Cancer Invasive Front. *Cell* **183**, 838, doi:10.1016/j.cell.2020.10.021 (2020).

26   Bajema, I. M. *et al.* Revision of the International Society of Nephrology/Renal Pathology Society classification for lupus nephritis: clarification of definitions, and modified National Institutes of Health activity and chronicity indices. *Kidney Int* **93**, 789-796, doi:10.1016/j.kint.2017.11.023 (2018).

27   Schubert, E., Sander, J., Ester, M., Kriegel, H. P. & Xu, X. DBSCAN revisited, revisited: why and how you should (still) use DBSCAN. *ACM Transactions on Database Systems (TODS)* **42**, 1-21 (2017).

28   Bolognesi, M. M. *et al.* Multiplex Staining by Sequential Immunostaining and Antibody Removal on Routine Tissue Sections. *J Histochem Cytochem* **65**, 431-444, doi:10.1369/0022155417719419 (2017).

29   McKinney, E. F., Lee, J. C., Jayne, D. R., Lyons, P. A. & Smith, K. G. T-cell exhaustion, co-stimulation and clinical outcome in autoimmunity and infection. *Nature* **523**, 612-616, doi:10.1038/nature14468 (2015).

30   Tilstra, J. S. *et al.* Kidney-infiltrating T cells in murine lupus nephritis are metabolically and functionally exhausted. *J Clin Invest* **128**, 4884-4897, doi:10.1172/jci120859 (2018).

31   Bocharnikov, A. V. *et al.* PD-1hiCXCR5- T peripheral helper cells promote B cell responses in lupus via MAF and IL-21. *JCI insight* **4**, doi:10.1172/jci.insight.130062 (2019).

32   Rao, D. A. *et al.* Pathologically expanded peripheral T helper cell subset drives B cells in rheumatoid arthritis. *Nature* **542**, 110-114, doi:10.1038/nature20810 (2017).

33   Liu, Z. & Davidson, A. Taming lupus-a new understanding of pathogenesis is leading to clinical advances. *Nat Med* **18**, 871-882 (2012).

34   Dooley, M. A. *et al.* Effect of belimumab treatment on renal outcomes: results from the phase 3 belimumab clinical trials in patients with SLE. *Lupus* **22**, 63-72, doi:10.1177/0961203312465781 (2013).

35   Mysler, E. F. *et al.* Efficacy and safety of ocrelizumab in active proliferative lupus nephritis: results from a randomized, double-blind, phase III study. *Arthritis Rheum* **65**, 2368-2379, doi:10.1002/art.38037 (2013).

36   Rovin, B. H. *et al.* Efficacy and safety of rituximab in patients with active proliferative lupus nephritis: the Lupus Nephritis Assessment with Rituximab study. *Arth Rheum* **64**, 1215-1226 (2012).

37   Almaani, S. & Rovin, B. H. B-cell therapy in lupus nephritis: an overview. *Nephrol Dial Transplant* **34**, 22-29, doi:10.1093/ndt/gfy267 (2019).

38   Levy, R. A. *et al.* 10 Years of belimumab experience: What have we learnt? *Lupus*, 9612033211028653, doi:10.1177/09612033211028653 (2021).

39   Atisha-Fregoso, Y. *et al.* Phase II Randomized Trial of Rituximab Plus Cyclophosphamide Followed by Belimumab for the Treatment of Lupus Nephritis. *Arthritis Rheumatol* **73**, 121-131, doi:10.1002/art.41466 (2021).

40   Furie, R. *et al.* Two-Year, Randomized, Controlled Trial of Belimumab in Lupus Nephritis. *N Engl J Med* **383**, 1117-1128, doi:10.1056/NEJMoa2001180 (2020).

41   Li, H. *et al.* Systemic lupus erythematosus favors the generation of IL-17 producing double negative T cells. *Nat Commun* **11**, 2859, doi:10.1038/s41467-020-16636-4 (2020).

42   Crispín, J. C. *et al.* Expanded double negative T cells in patients with systemic lupus erythematosus produce IL-17 and infiltrate the kidneys. *J Immunol* **181**, 8761-8766, doi:10.4049/jimmunol.181.12.8761 (2008).

43   Paul, S., Shilpi & Lal, G. Role of gamma-delta (γδ) T cells in autoimmunity. *J Leukoc Biol* **97**, 259-271, doi:10.1189/jlb.3RU0914-443R (2015).

44   Bank, I. The Role of Gamma Delta T Cells in Autoimmune Rheumatic Diseases. *Cells* **9**, doi:10.3390/cells9020462 (2020).

45   Kaminski, H., Couzi, L. & Eberl, M. Unconventional T cells and kidney disease. *Nat Rev Nephrol*, doi:10.1038/s41581-021-00466-8 (2021).

46   Deng, Q. *et al.* The Emerging Epigenetic Role of CD8+T Cells in Autoimmune Diseases: A Systematic Review. *Front Immunol* **10**, 856, doi:10.3389/fimmu.2019.00856 (2019).

47   Rovin, B. H. *et al.* Efficacy and safety of voclosporin versus placebo for lupus nephritis (AURORA 1): a double-blind, randomised, multicentre, placebo-controlled, phase 3 trial. *Lancet* **397**, 2070-2080, doi:10.1016/s0140-6736(21)00578-x (2021).

48   Fassbinder, T. *et al.* Differential effects of cyclophosphamide and mycophenolate mofetil on cellular and serological parameters in patients with systemic lupus erythematosus. *Arthritis Res Ther* **17**, 92, doi:10.1186/s13075-015-0603-8 (2015).

49   Banchereau, R. *et al.* Personalized Immunomonitoring Uncovers Molecular Networks that Stratify Lupus Patients. *Cell* **165**, 551-565, doi:10.1016/j.cell.2016.03.008 (2016).

50   Blanco, P., Palucka, A. K., Gill, M., Pascual, V. & Banchereau, J. Induction of dendritic cell differentiation by IFN-alpha in systemic lupus erythematosus. *Science* **294**, 1540-1543, doi:10.1126/science.1064890 (2001).

51   Baechler, E. C. *et al.* Interferon-inducible gene expression signature in peripheral blood cells of patients with severe lupus. *Proc Natl Acad Sci U S A* **100**, 2610-2615, doi:10.1073/pnas.0337679100 (2003).

52   Niewold, T. B., Clark, D. N., Salloum, R. & Poole, B. D. Interferon Alpha in Systemic Lupus Erythematosus. *Journal of Biomedicine and Biotechnology* **2010**, 948364, doi:10.1155/2010/948364 (2010).

53   Furie, R. A. *et al.* Type I interferon inhibitor anifrolumab in active systemic lupus erythematosus (TULIP-1): a randomised, controlled, phase 3 trial. *The Lancet Rheumatology* **1**, e208-e219, doi:10.1016/S2665-9913(19)30076-1 (2019).

54   Khamashta, M. *et al.* Sifalimumab, an anti-interferon-α monoclonal antibody, in moderate to severe systemic lupus erythematosus: a randomised, double-blind, placebo-controlled study. *Ann Rheum Dis* **75**, 1909-1916, doi:10.1136/annrheumdis-2015-208562 (2016).

55   Morand, E. F. *et al.* Trial of Anifrolumab in Active Systemic Lupus Erythematosus. *N Engl J Med* **382**, 211-221, doi:10.1056/NEJMoa1912196 (2020).

56   Fiore, N. *et al.* Immature myeloid and plasmacytoid dendritic cells infiltrate renal tubulointerstitium in patients with lupus nephritis. *Mol Immunol* **45**, 259-265 (2008).

57   Parikh, S. V. *et al.* A Novel Inflammatory Dendritic Cell That Is Abundant and Contiguous to T Cells in the Kidneys of Patients With Lupus Nephritis. *Front Immunol* **12**, 621039, doi:10.3389/fimmu.2021.621039 (2021).

58   He, K., Gkioxari, G., Dollár, P. & Girshick, R. in *Proceedings of the IEEE international conference on computer vision.* 2961-2969.

59   Simonyan, K. & Zisserman, A. Very deep convolutional networks for large-scale image recognition. *arXiv preprint arXiv:1409.1556* (2014).
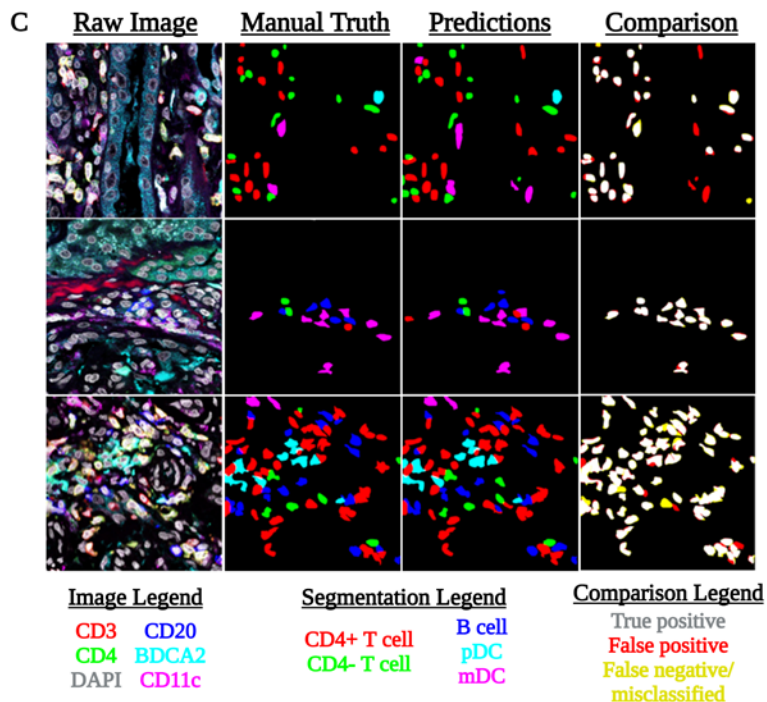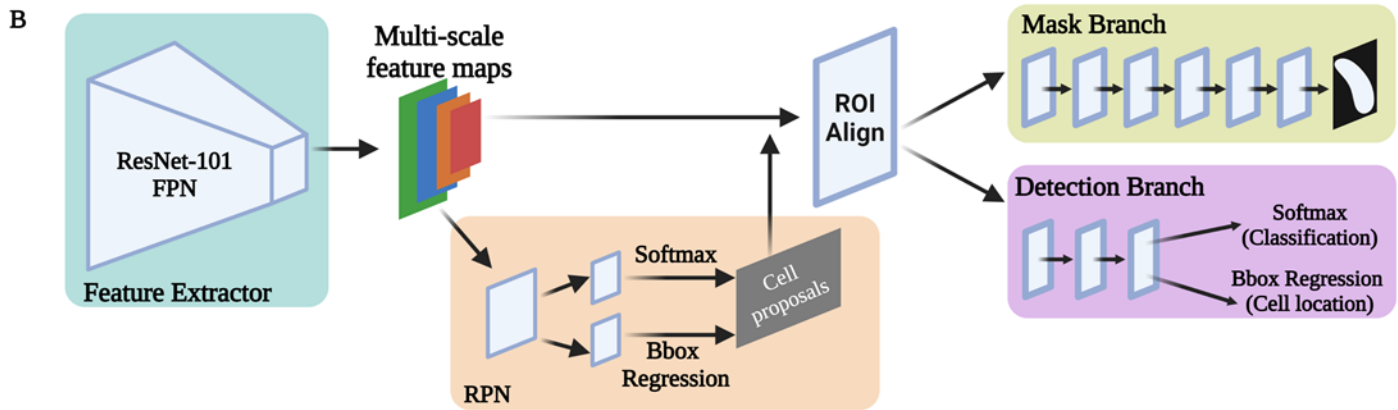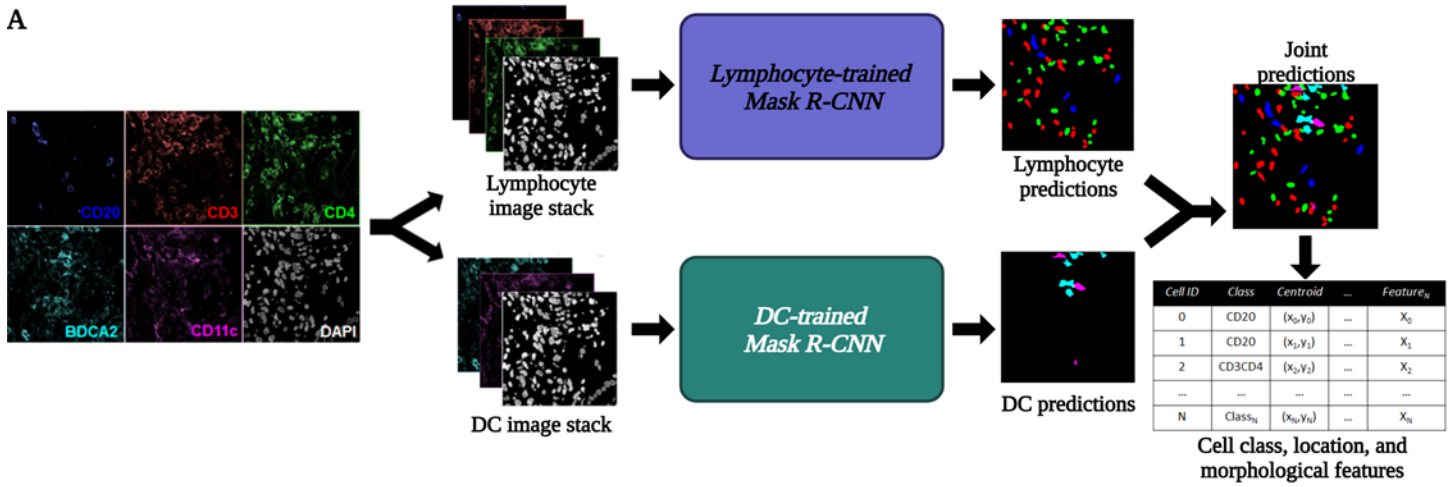
Figure 1. Instance segmentation of immune cells in high-resolution fluorescence microscopy images of LN kidney biopsies. A) Automatic instance segmentation of five immune cell classes was performed by combining predictions from two instances of Mask R-CNN: one trained to segment CD20+, CD3+CD4-, and CD3+CD4+ lymphocytes and one trained to segment pDCs and mDCs. Cell location, class, and morphological features were calculated from joint predictions. B) The Mask R-CNN architecture is comprised of a ResNet Feature Pyramid Network (FPN) backbone used for feature extraction, a region proposal network (RPN) used to generate cell proposals, and two parallel branches used for 1) semantic segmentation (mask branch), and 2) classification (softmax layer) and localization (bounding box (Bbox) regression) of cell proposals. C) Representative segmentations produced by the multi-network pipeline showed strong agreement with the expert-defined manual segmentations.
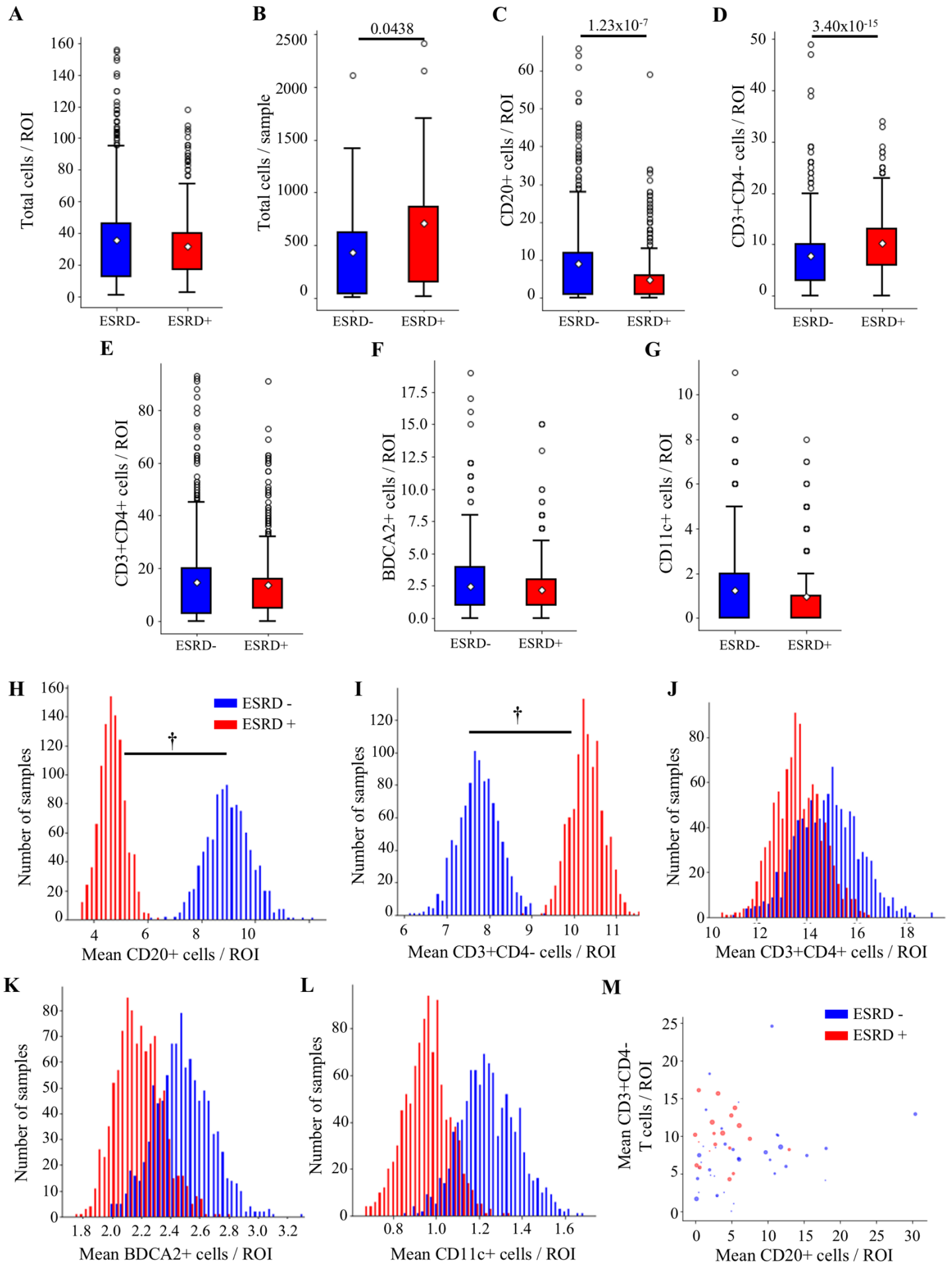
Figure 2. Higher CD4- T cell density and lower B cell density associated with progression to ESRD. Difference in the number of indicated cell classes per ROI between patients who progressed to ESRD (ESRD+, n=428 ROIs) and those who do not (ESRD-, n=437 ROIs) for A) Total cells per ROI across the HR dataset (p=0.318), B) Total cells per patient sample, C) CD20+ cells per ROI, D) CD3+CD4- cells per ROI, E) CD3+CD4+ cells per ROI, F) BDCA2+ cells per ROI, G) CD11c+ cells per ROI. All cell density comparisons were done with a Mann-Whitney U Test with a Bonferroni correction for multiple comparisons. Significant p values noted in the plots. Bootstrapped sample means of ESRD+ (red) and ESRD-(blue) for H) CD20+ cells per ROI, I) CD3+CD4- cells per ROI, J) CD3+CD4+ cells per ROI, K) BDCA2+ cells per ROI, and L) CD11c+ cells per ROI. Average B cell and CD4- T cell count per ROI for each patient biopsy is shown in (M). Point size is weighted by the TI chronicity score for each patient. († 95% confidence interval does not overlap with 0)
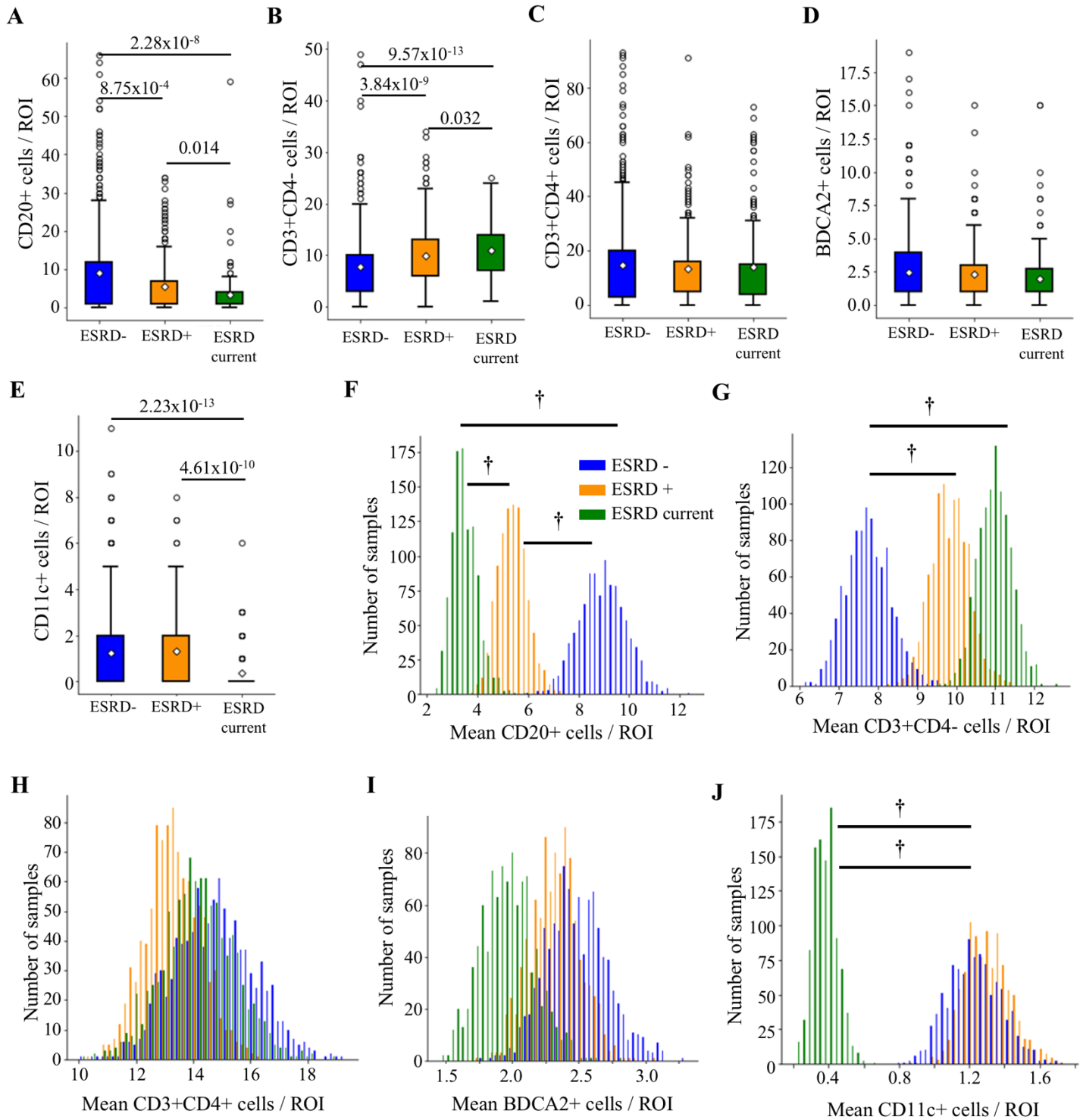
Figure 3. Local cell densities are associated with progressively worse renal outcomes. Difference in the number of cells of each class per ROI from patients who did not progress to ESRD (ESRD-, n=437 ROIs), people who progressed to ESRD > 2 weeks post-biopsy (ESRD+, n=266), and people who progressed to ESRD within 2 weeks of the biopsy date (ESRD current, n=162). A) CD20+ cells/ROI, B) CD3+CD4- cells/ROI, C) CD3+CD4+ cells/ROI, D) BDCA2+ cells/ROI, E) CD11c+ cells/ROI. All cell density comparisons were done with a Mann-Whitney U Test with a Bonferroni correction for multiple comparisons. Significant p values noted in the plots. Bootstrapped means of samples of ESRD- (blue), ESRD+ (orange), and ESRD current (green) ROIs for F) CD20+ cells/ROI, G) CD3+CD4- cells/ROI, H) CD3+CD4+ cells/ROI, I) BDCA2+ cells/ROI, J) CD11c+ cells/ROI. († 95% confidence interval does not overlap with 0)
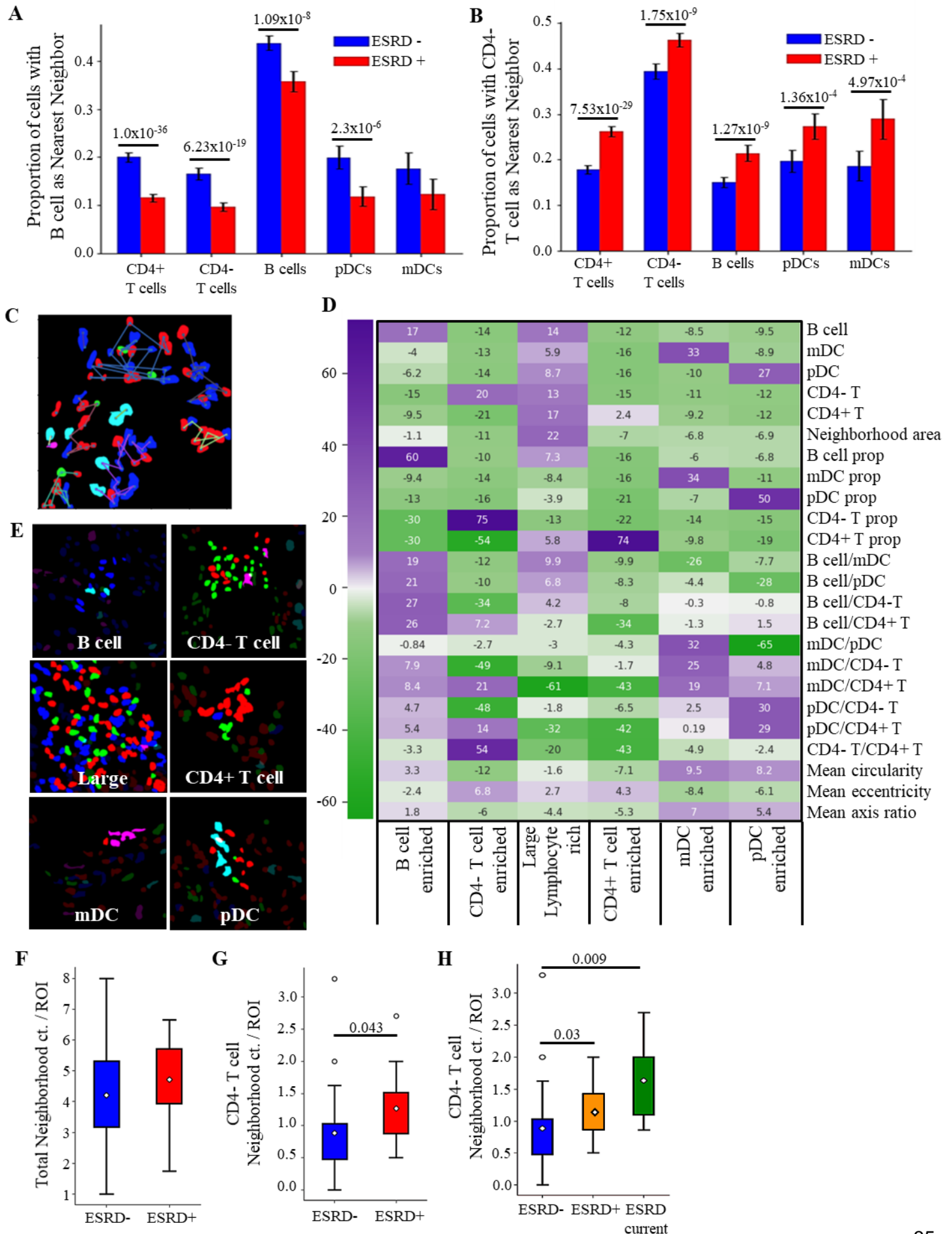
Figure 4. Specific cellular neighborhoods associated with renal failure. Proportions of cells that have A) CD3+CD4- T cells and B) CD20+ B cells as nearest neighbors in ESRD+ and ESRD- patients (chi-squared test for independence with Bonferroni correction for multiple comparisons, significant p values noted in the plots). C) Representative neighborhoods detected by the DBSCAN with a distance metric of $\leq$ 100 pixels. D) Heatmap showing test statistics for each features from leave-one-out t-tests used to define six types of cell neighborhoods. E) Representative neighborhoods of each cluster. The abundance of neighborhoods between the patient cohorts, normalized by the number of ROIs per patient, is compared by Mann-Whitney U Test, with a Bonferroni correction for F) all cell neighborhoods, G) CD4- T cell neighborhoods; A 3-group comparison for CD4- neighborhoods, splitting the ESRD+ population into ESRD+ and ESRD current patients is shown in (H). Significant p values noted in the plots.
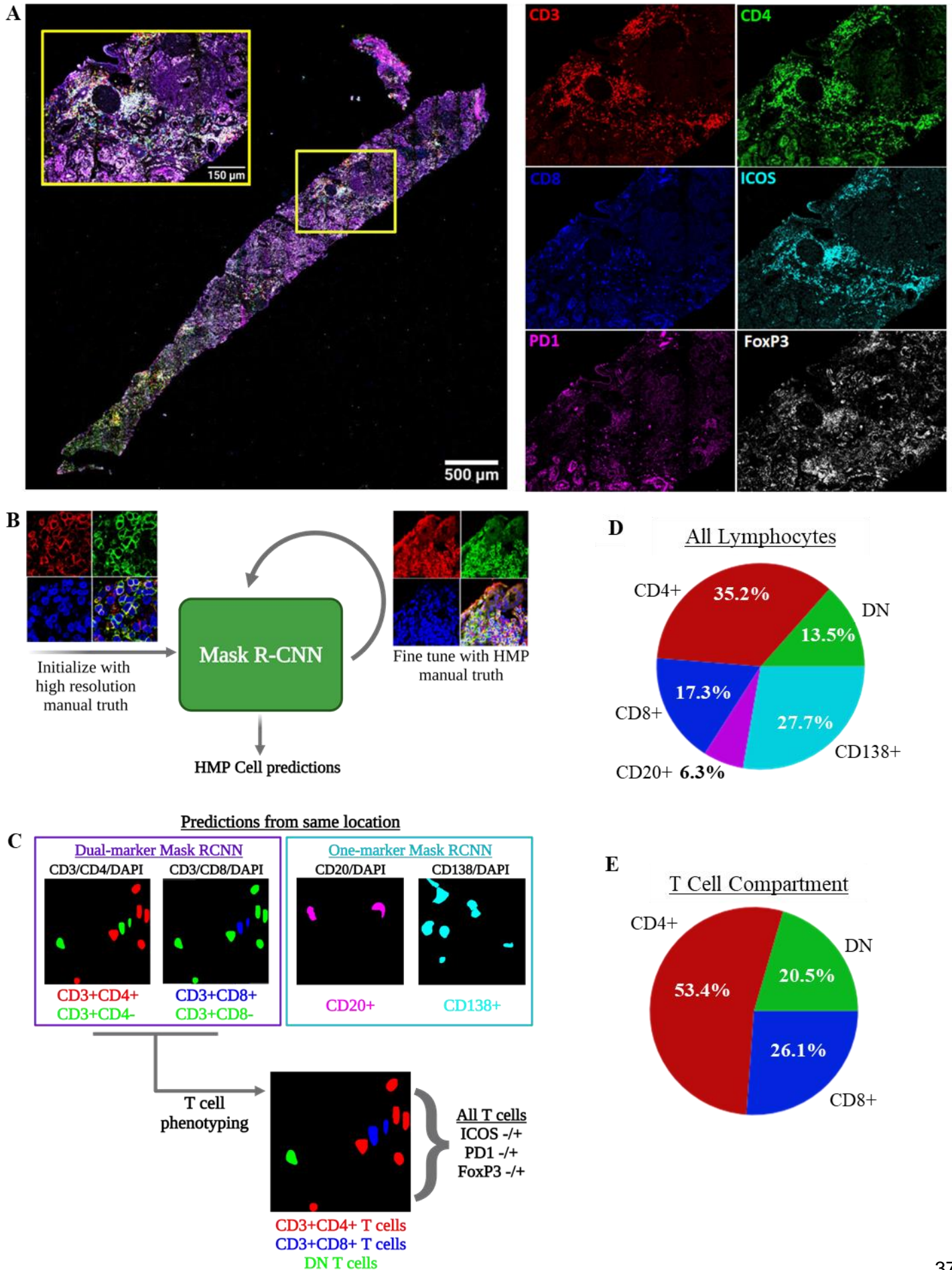
Figure 5. Cell detection, segmentation, and phenotyping in highly multiplexed fluorescence microscopy images. A) Representative composite of a full biopsy section, shown with merged and with isolated panels of CD3, CD4, CD8, ICOS, PD1, and FoxP3. B) Schematic of procedure for training and fine-tuning a Mask R-CNN for instance segmentation of cells in highly multiplexed microscopy images. C) Cell predictions from Mask R-CNNs trained for dual-marker and single-marker cell detection are used to establish base lymphocyte classes. All T cell predictions are further described by ICOS, PD1, and FoxP3 expression. D) Breakdown of frequencies of the five base classes in the HMP dataset. E) Frequencies of CD4, DN and CD8 T cells within the T cell compartment.
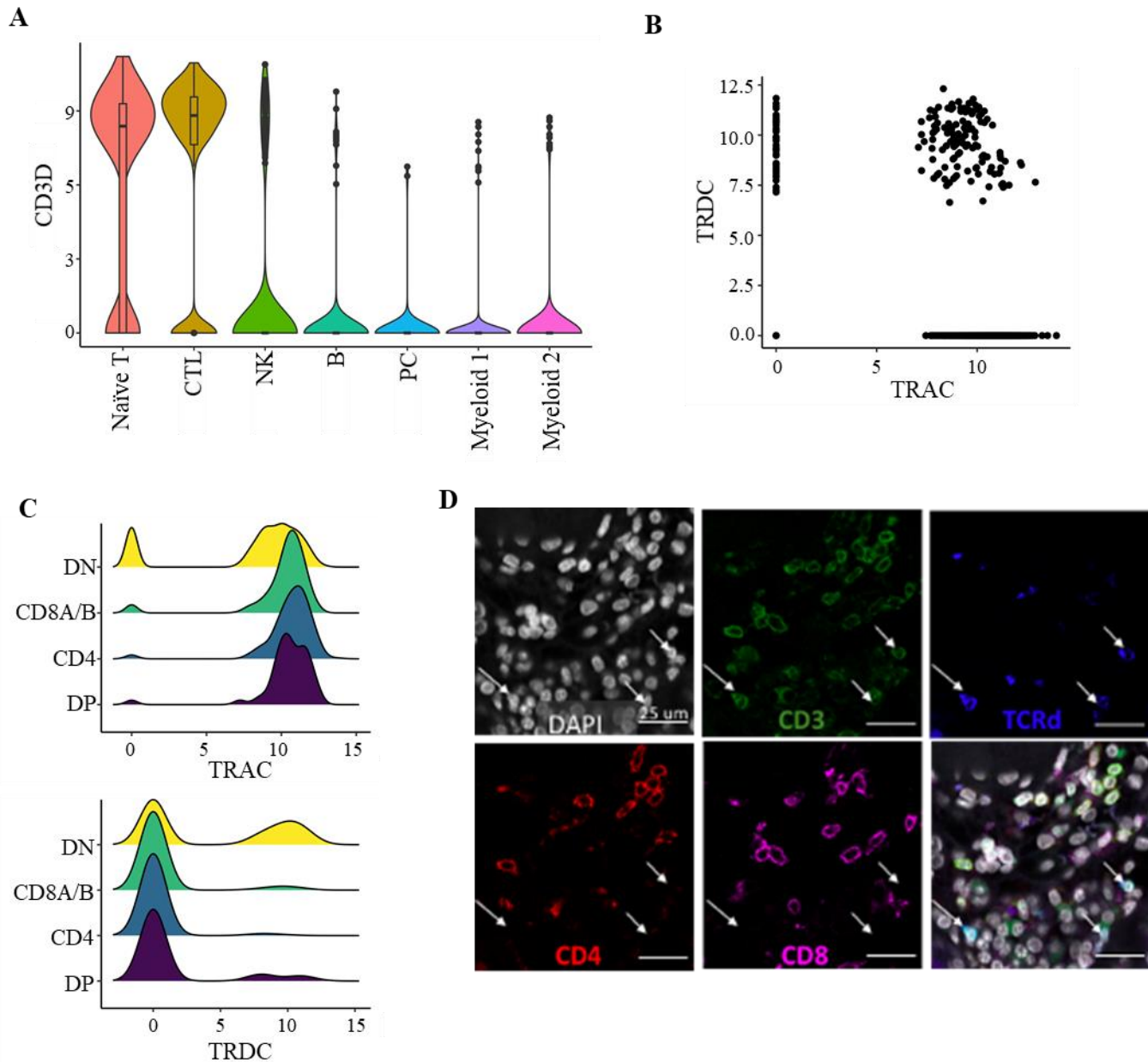
Figure 6. Identifying $\gamma\delta$ T cells in LN. A) distribution of *CD3D* in cell clusters identified in scRNA-Sequencing data from LN kidney samples, B) expression of *TRAC* and *TRDC* in T cells identified in scRNA-Seq data, C) comparison of *TRAC* and *TRDC* expression in identified DN, CD8+, CD4+ and DP T cells, D) representative image of double negative (CD4-CD8-) $\gamma\delta$ (TCRd+) T cells in LN biopsy, marked by white arrows.
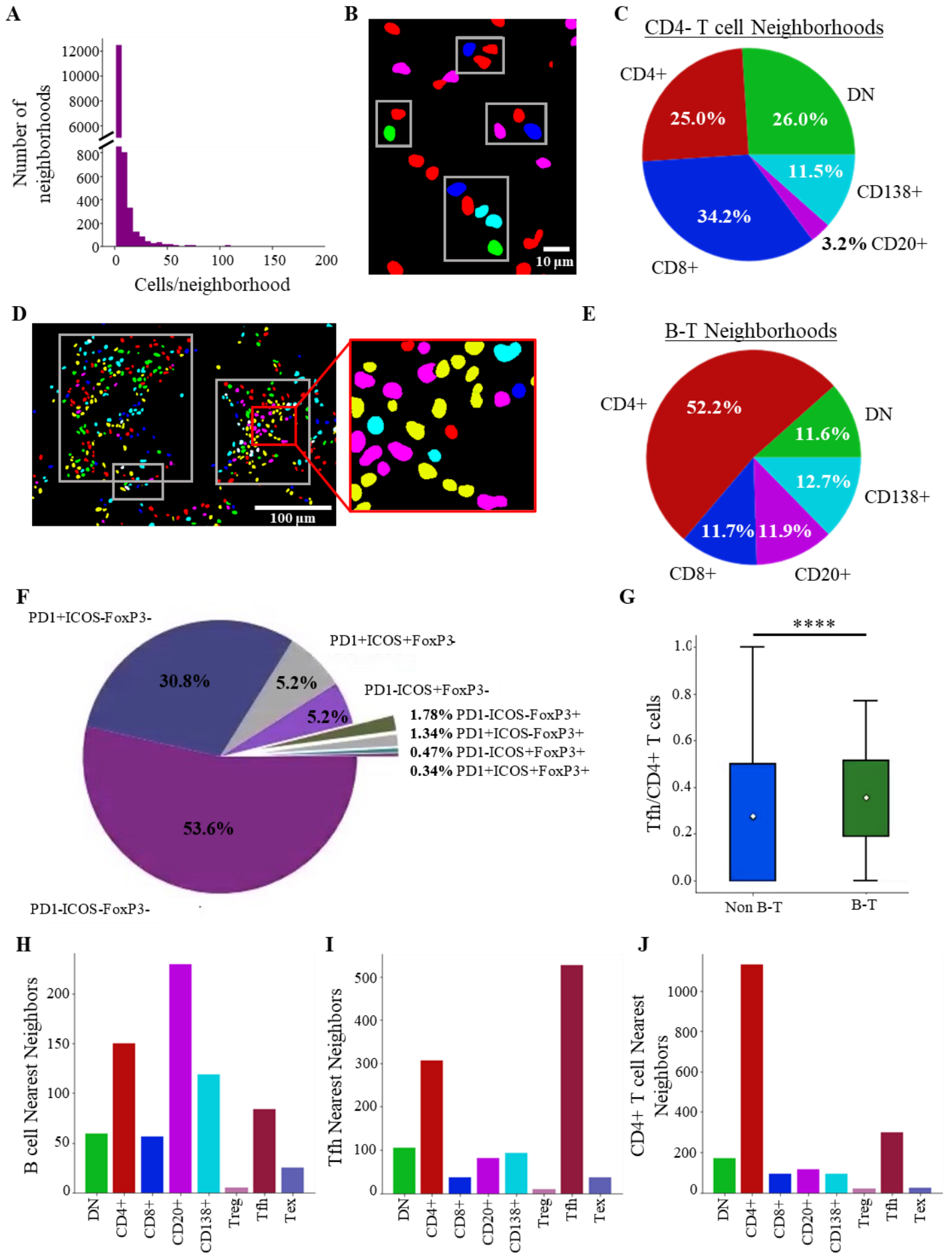
Figure 7. Identification of distinct CD4- and B-T neighborhoods; A) Distribution of sizes of all cell neighborhoods in the HMP dataset. B) Representative composite of CD4-clusters, red=CD4+ T cells, blue=CD8+ T cells, green=DN T cells. C) Distribution of the five main lymphocyte classes in the CD4-T cell neighborhoods. D) Representative composite showing identified B-T aggregates (outlined by white boxes), green=DN, red =non-Tfh CD4+, yellow=Tfh; blue=CD8+, magenta =CD20+,cyan = CD138+ cells. E) Distribution of frequencies of the five base classes of lymphocytes in B-T neighborhoods. F) Distribution of CD4+ T cell phenotypes in B-T neighborhoods. G) Comparison of proportion of CD4+ T cells that are Tfh in identified B-T aggregates and non B-T aggregates (Mann-Whitney U Test, p =1.9×10^{-6}). The nearest neighbors of H) CD20+ B cells, I) Tfh, and J) CD4+ T cells within B-T aggregates.
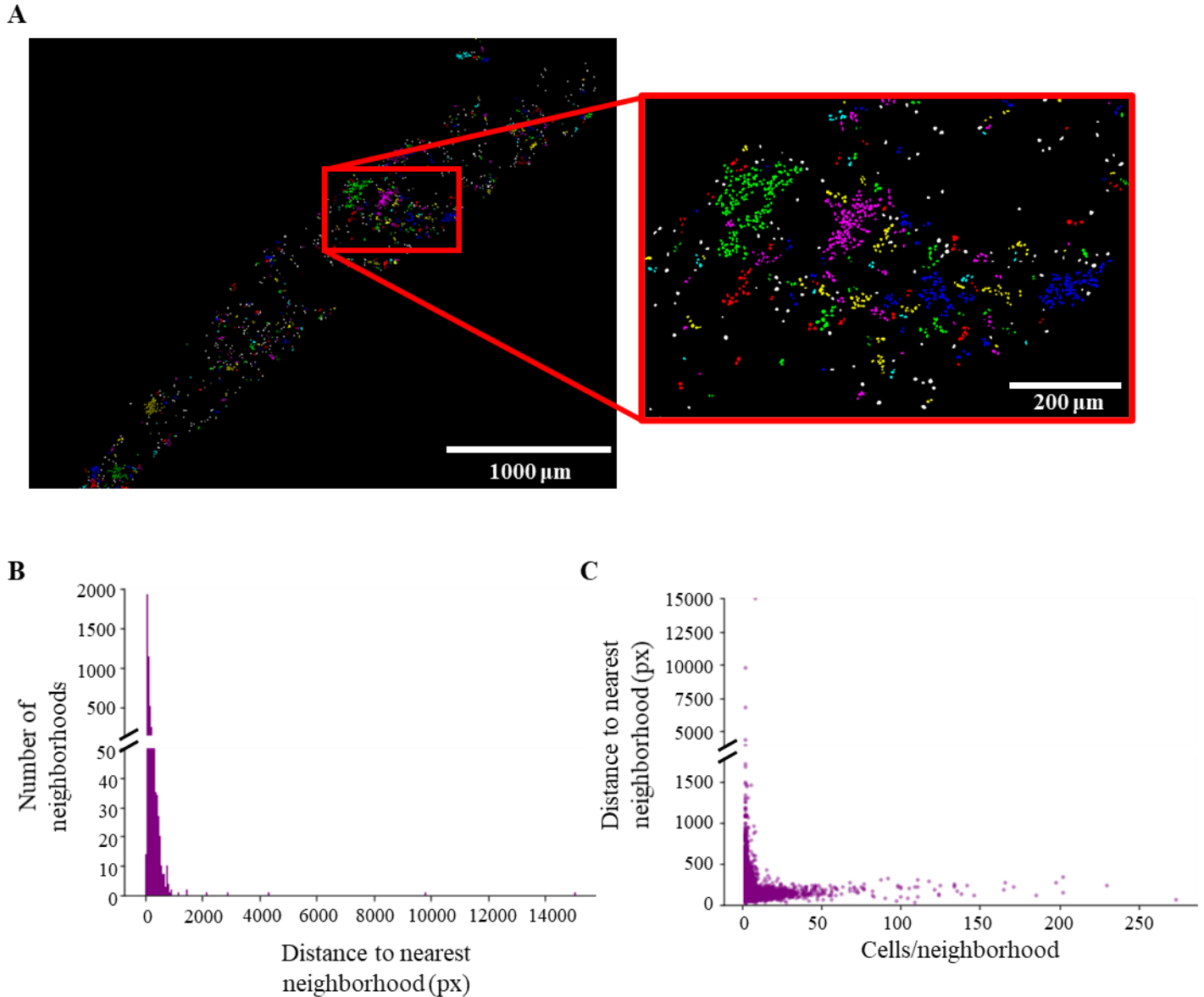
Figure 8. Large cell neighborhoods congregate to form cell "cities". A) Representative image of neighborhood detection in a full-biopsy section from highly multiplexed microscopy data, inset: segmented cells are color-coded based on neighborhood assignment. B) Distribution of minimum distance of a given neighborhood to another neighborhood. C) Relationship between cells per neighborhood and distance to another neighborhood.